Reconstruction of Magnetic Configurations in W7-X using Artificial Neural Networks

Daniel Böckenhoff[1], Marko Blatzheim[1, 2], Hauke Hölbe[1], Holger Niemann[1], Fabio Pisano[3], Roger Labahn[2], Thomas Sunn Pedersen[1] and the W7-X Team[1]

[1]Max Planck Institute for Plasma Physics, Wendelsteinstraße 1, 17491 Greifswald, Germany
[2]Institute for Mathematics, University of Rostock, Ulmenstraße 69, 18057 Rostock, Germany
[3]Department of Electrical and Electronic Engineering, University of Cagliari, Via Marengo 2, 09123 Cagliari, Italy

*daniel.boeckenhoff@ipp.mpg.de*, *marko.blatzheim@ipp.mpg.de*

Abstract

It is demonstrated that artificial neural networks can be used to accurately and efficiently predict details of the magnetic topology at the plasma edge of the Wendelstein 7-X stellarator, based on simulated as well as measured heat load patterns onto plasma-facing components observed with infrared cameras. The connection between heat load patterns and the magnetic topology is a challenging regression problem, but one that suits artificial neural networks well. The use of a neural network makes it feasible to analyze and control the plasma exhaust in real-time, an important goal for Wendelstein 7-X, and for magnetic confinement fusion research in general.

1 Introduction

Wendelstein 7-X (W7-X) is a pioneering experiment of the latest generation of optimized stellarators [1, 2]. It aims to demonstrate steady state capability of the confinement concept with plasma parameters near those required in an energy-producing fusion reactor [3, 4], and to demonstrate the steady-state capabilities of stellarators also at these parameters. The experiment started operation (Operation Phase 1.1, OP1.1) in 2015 [5], has started its next operation phase (OP1.2) in 2017, and will, when the water-cooled plasma-facing components have been fully installed in operation phase 2 (OP2), have discharge times of 30 min with continuous injected power of up to 10 MW. This discharge duration is about an order of magnitude longer than the longest characteristic time scale of the plasma, which is the one on which the net toroidal current, I_{tor}, evolves. The dominant contributor to I_{tor} is the bootstrap current I_{bs}, and the time evolution of I_{tor} can be approximated as: $I_{\text{tor}} = I_{\text{bs}} \cdot e^{-\frac{t}{\tau}}$ with L/R-time τ being the L/R time scale, of order 1 min for high-performance plasmas.

On these time scales, power exhaust is an important issue. Ten specially designed discrete island divertor modules [6] take the major part of heat flux that passes the Last Closed Magnetic Surface (LCMS), which defines the edge of the confined plasma. The actively cooled divertors, necessary for OP2, are designed to sustain local power loads up to 10 MW/m². Other first wall components, however, can only be loaded with a fraction of this heat flux, e.g. the less cooled divertor edge withstands roughly 3 MW/m² [7, 8]. Overloading the divertors implies a risk of delamination, water leaks (cf. [9, 10]) and impurity buildup, partially as a consequence of the first two, and must therefore be avoided.

To ensure the safety of the first wall, in particular the divertor, and to protect the plasma from impurities, real-time control is highly desirable, in particular for steady-state oper-
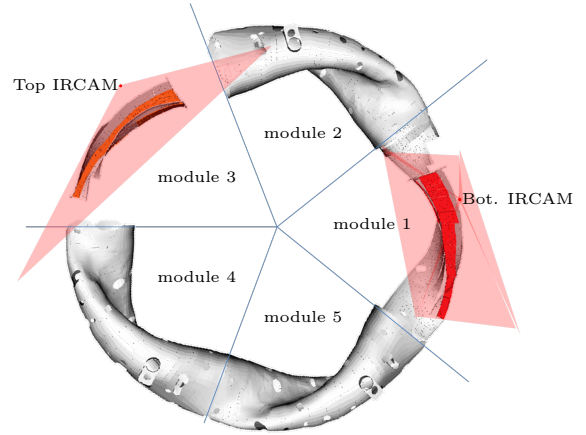

(a) *Divertor setup with cutaways in modules one and three as used in OP1.2 and afterwards. Depicted are only two of the 10 divertors and the associated IRCAMS. Module one only reveals the top divertor while module three shows the bottom divertor.*
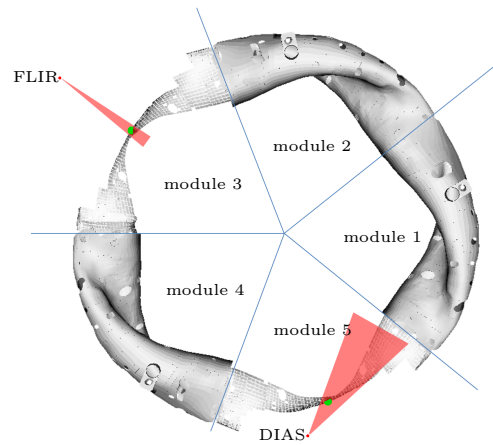
(b) *Limiter setup with cutaways in modules three and five as used in OP1.1. On this scale and view, the limiters are small (green).*

Figure 1: *Top-down CAD views of the W7-X inner vessel, showing sight lines of the IR camera systems in the two differing setups.*
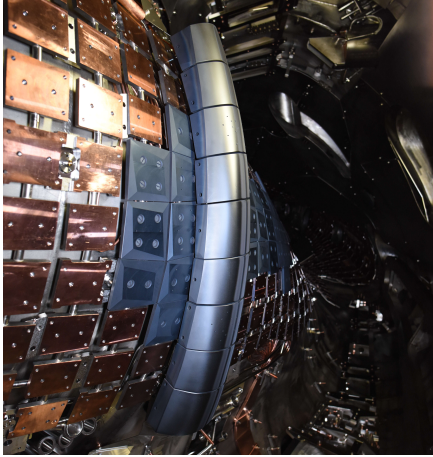
Figure 2: *Side view of the W7-X limiter in module 5 after OP1.1*

ation. An important part of such a real-time control system would be one that optimizes elements of the divertor operation, such as pumping performance and detachment. We aim to develop and ultimately implement such a feedback controller in the device operation system.

The most important sensor system for this control loop will be ten endoscopes that will allow IR and visible observation of the ten divertor units. Prototypes of these will be in operation in the now running intermediate operation phase OP1.2, each observing one divertor [11] (cf. Figure 1a). In OP1.1 five graphite limiters were placed vertically in the bean shaped cross section of the plasma vessel (cf. Figure 1b). In the confinement region, the magnetic field lines form nested toroidal surfaces that are not intersected by material objects. The aforementioned LCMS marks the transition to the exhaust region, called the Scrape-Off Layer (SOL) which is characterized by field lines that do intersect material objects, the Plasma-Facing Components (PFCs). The plasma enters the SOL through diffusive and convective transport processes perpendicular to the magnetic field, and then enters and populates the SOL field lines. These guide the outflowing plasma heat and particles to the PFCs. A common term for the shape- and intensity distribution of the resulting heat load pattern on the PFCs is "strike line" since it is

usually highly elongated. A complex interplay of component shape, magnetic field structure, cross- and parallel field transport results in the strike lines observed.

The IR camera views of the strike-line patterns have a complicated relationship with the magnetic topology and the transport processes in the plasma and the main task for such a feedback system is the abstraction and real time processing of these camera images which are being recorded at frame rates of 50 Hz. Artificial Neural Networks (NN, see Section 2.1) have significantly improved in the last ten years and should be well suited for this task.

A machine learning approach for real time control is an active object of research in the nuclear fusion community for several different tasks [12–14].

The first step towards the ambitious goal of controlling the plasma divertor operation for W7-X in real-time is presented here: the training of NNs to reconstruct the edge magnetic topology from IR camera observations of the strike-lines.

So far, IR picture series are available from OP1.1 discharges only (cf. Section 2.4.1), with OP1.2 barely started at the time of writing this paper. With a very limited set of different magnetic configurations, these experimental data available is no solid basis for a NN training set. To alleviate this problem, simulated strike lines function as NN training set data, and the performance of the NN is verified with experimental data. Since in OP1.1 no divertor was installed only the aforementioned limiters, this study is done entirely with the OP1.1 limiter geometry and associated magnetic configurations.

The limiters are centered on planes with up-down symmetry, which reduces the geometric complexity of the strike line. Complexity of the intersection between magnetic field and limiter is moreover minimized by limiter design. These two factors restrain the limiter strike line variability to a fraction of the divertor strike line. Because of this, the mag-

netic configuration reconstruction from limiter strike lines is expected to be much less accurate than that of more variable divertor strike lines.

The relevant information regarding the used NN architecture, W7-X, training data creation and NN input pre-processing are given in Section 2. In Section 3 we present the results of the challenging magnetic field reconstruction from limiter strike lines, which give reason for optimism with respect to future performance in a divertor geometry.

ers (see Figure 4a), where an input vector $\vec{x}$ is linearly transformed, followed by an element wise non-linearity ϕ, usually referred to as activation function (see Figure 3) such that

$$f\left(\vec{x}\right) = \phi\left(\boldsymbol{W}\vec{x} + \vec{b}\right) \tag{1}$$
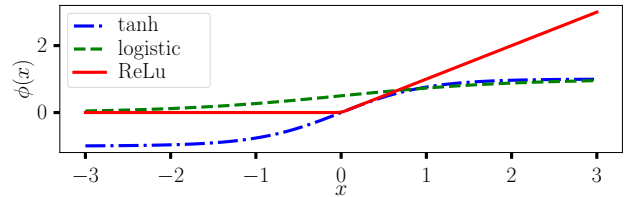
Figure 3: *Activation functions*

2 Methods

2.1 Artificial Neural Network

Machine learning tackles the question "How can we build computer systems that automatically improve with experience, and what are the fundamental laws that govern all learning processes?" as stated by Tom Mitchel in [15]. Artificial Neural Networks are an approach to solving machine learning problems. This capability allows them to reproduce the behavior of unknown, complicated functions from many examples instead of explicitly programming the function traditionally. The NNs used to predict the magnetic configuration are all based on ideas from 1975, when the method of backpropagation for NNs was introduced [16]. Such a NN depends on numerous parameters that are optimized in a so-called training process. In the previous decades NNs were not as popular as they have now become, especially because the parameter convergence during the training turned out to be slow and the amount of training data was small. Recently NNs are used more frequently because of newly developed network architectures [17, 18], the improvement of NN training algorithms [19, 20], increased computer performance [21] and open source NN libraries [22, 23].
A simple NN is based on fully connected lay-

represents one layer. The free parameters $\boldsymbol{W}$ and $\vec{b}$ define the linear transformation. The activation function mimics the transmission of action potential in physiological neurons, which only create a signal if a certain threshold potential is reached. It is crucial to choose ϕ so that it is smooth and differentiable almost everywhere to allow an efficient gradient-based optimization. A NN consists of multiple of such or more complex layers where the output of one layer is treated as the input of the following one.
A more complex layer is the so-called convolutional layer [24], which has been developed to recognize patterns independent of the location by applying the same linear transformation on multiple smaller subsets of the input. Another positive effect is the reduction of free parameters, which decreases the risk of overfitting [25]. Convolutional layers (see Figure 4b) are used particularly frequently in image pattern recognition. For example the AlexNet architecture [26], which successfully won the 2012 ImageNet challenge [27], consists of several such layers. Most more complex layer structures, that are not recurrent, are based on the concept of convolutional layers.
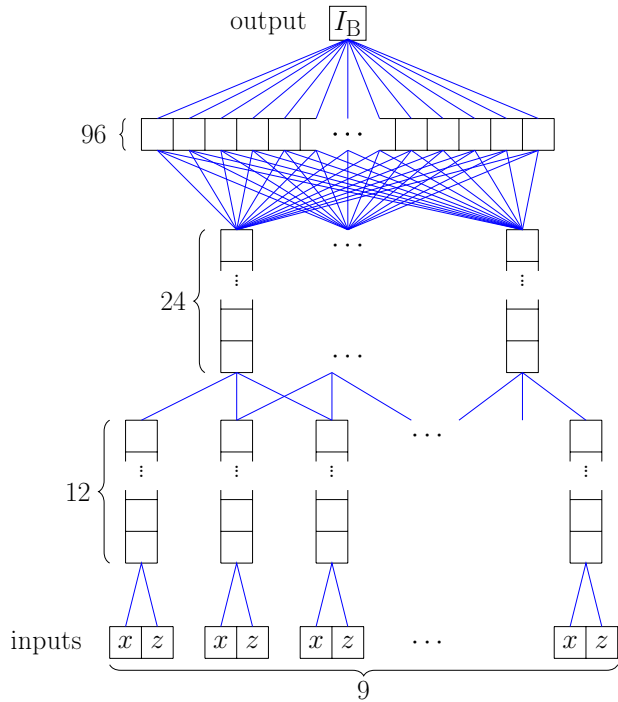The free parameters are arranged in the vector
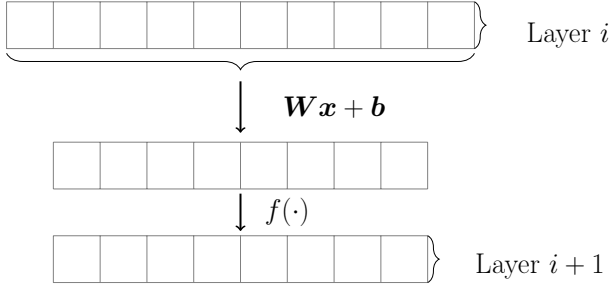
(a) *Fully connected layer*
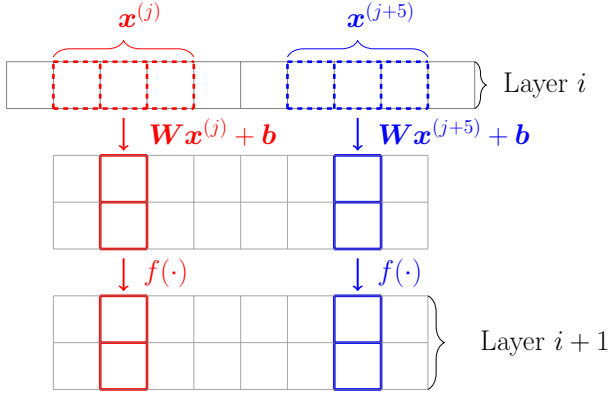
(b) *1D convolutional layer with kernel size 3 and 2 output feature maps*

Figure 4: *Schematic representation of neural network layer architectures*

Figure 5: *The used neural network architecture with two convolutional layers and two fully connected layers*

$\vec{\theta}$. To train the NN, the error

$$E\left(\vec{\theta}\right) = \sum_{i=1}^{N} \left(y(\vec{x}_i, \vec{\theta}) - y_i^{\text{target}} \right)^2, \qquad (2)$$

defined as the sum of squared differences between all NN result values $y(\vec{x}_i, \vec{\theta})$ with inputs $\vec{x}_i$ and target values y_i^{target} of the corresponding set with set size N, is minimized with respect to all free parameters. By calculating $\vec{\nabla}_\theta E$, the gradient of the error with respect to $\vec{\theta}$, efficient gradient based minimization algorithms can be used. The basic approach is the gradient descent

$$\vec{\theta}_{i+1} = \vec{\theta}_i - \lambda \vec{\nabla}_\theta E \qquad (3)$$

with step size λ. This algorithm starts with an initial $\vec{\theta}_0$ and calculates new $\vec{\theta}_{i+1}$ with every iteration.

The data set is separated in training, validation and test sets. Weights are adjusted with the training set only. Training terminates if the error on the validation set reaches a minimum. Once the NN training stops, the generalization quality is checked on the independent test set. To increase the rate of convergence, this method has been improved by the stochastic gradient descent where the error gradient is not calculated for all training sets but only for a stochastic selection, the mini-batch. After each mini-batch θ is updated. Other improvements focus on the choice of $\vec{\theta}_0$ [28] or the step size λ, where, instead of a constant value, an adaptive method depending on the previous λ and the derivative $\vec{\nabla}_\theta E$, such as AdaGrad [19] and Adam [20], determines the update rule.

Though in the W7-X experiment IR cameras will monitor the vessel wall temperature, the input for the used NN is not an image, but characteristics extracted from it, as further explained in Section 2.4.3. Experimental data is scarce so the main data set is based on simulations (see Section 2.4.2). The network structure (see Figure 5) consists of two 1D convolutional layers followed by two fully connected layers. This choice is based on the better performance as compared to fully connected layer based NNs. The convolutional

layers consist of 12 and 24 feature maps respectively, the first fully connected layer consists of 96 neurons. The last layer in this NN leads to the target value.

The network is trained with the Adam optimizer and the recommended parameters. A dropout [29] of 0.5 is applied during the training. The weights are initialized by a normal distribution with standard deviation 0.5 and 0.1 for the first three layers and the last layer respectively. The activation functions as introduced in Figure (3) are Rectified Linear Units (ReLU) in the convolutional layers. In the first fully connected layer the logistic function has been is chosen as activation function. Before the first layer, the NN input is linearly transformed in such a way, that the training set input has mean 0 and standard deviation 1 to improve convergence. The simulated data set has a size of 3993 and the experimental data set has a size of 319 cf. Table 2. The training set is nine times larger than the validation set while the test set size depends on the respective experiment.

The NN quality is evaluated by the root-mean-square error ($rmse$), defined as

$$rmse = \sqrt{\frac{E\left(\vec{\theta}\right)}{N}}. \qquad (4)$$

2.2 W7-X Coil System

Toroidal magnetic confinement devices need a rotational transform $\bar{\iota}$ to compensate for magnetic drifts which would otherwise cause charge separation. $\bar{\iota}$ is defined as

$$\bar{\iota} = c \cdot \frac{I_{\text{tor}}}{\Theta} + \bar{\iota}_{CF}, \qquad (5)$$

where

$$I_{\text{tor}} = \int_0^r j_{tor}(r') \frac{V(r')}{2\pi R_0} dr' \qquad (6)$$

is the toroidal current enclosed by the magnetic surface at r. $\Theta = \int \vec{\nabla}_\theta \vec{B} dV$ represents the toroidal magnetic flux. c denotes a constant that depends on the machine coil currents. $\bar{\iota}_{CF}$ is the current free part of $\bar{\iota}$, only

occurring in stellarators and as well depending on the coil geometry and currents [30].

The W7-X coil system is shown in Figure 6a. The magnetic coil system consists of five identical modules each of which is point symmetric towards the module center, creating a five-fold symmetry in the magnetic field (cf. Figure 6b). Each half module consists of five different non-planar and two planar coils, depicted in red and blue. The modular coils are used to confine the plasma. The planar coils provide further variability of the magnetic field.

The modular and planar coils consist of 108 and 36 windings respectively. For convenience and clearness, we indicate the corresponding coil currents $I_1, \ldots, I_5$ and I_A, I_B in terms of coil currents that would yield the same magnetic field with one winding only:

$$I_x = \frac{n_w \cdot I_{x,true}}{I_n}, \qquad (7)$$

$\forall x \in \{1, 2, \ldots, 5, A, B\}$, where the nominal current I_n is defined such, that all I_x are dimensionless. $I_{x,true}$ is the current that is actually applied to the coils and n_w denotes the number of windings per coil. This follows the convention used in [32].

The parameter space spanned by the coil currents is six-dimensional since the effects of the magnetic field strength are negligible.

2.3 Parameter Space Choice

The strike line is mainly influenced by the topology of the magnetic field $\vec{B}$ at the edge. The topology of $\vec{B}$ is to a large degree determined by the rotational transform $\bar{\iota}$ (cf. Section 2.2), which is a measure of how much a field line moves poloidally for one full toroidal turn. In stellarators, $\bar{\iota}$ is primarily determined by the currents in the magnetic coils rather than those running inside the plasma. We refer to this plasma-current free contribution as $\bar{\iota}_{CF}$. $\bar{\iota}$ is heavily dependent on the values of I_A and I_B. If $I_A + I_B < 0$, $\bar{\iota}$ is increased and vice versa. Plasma currents can similarly change
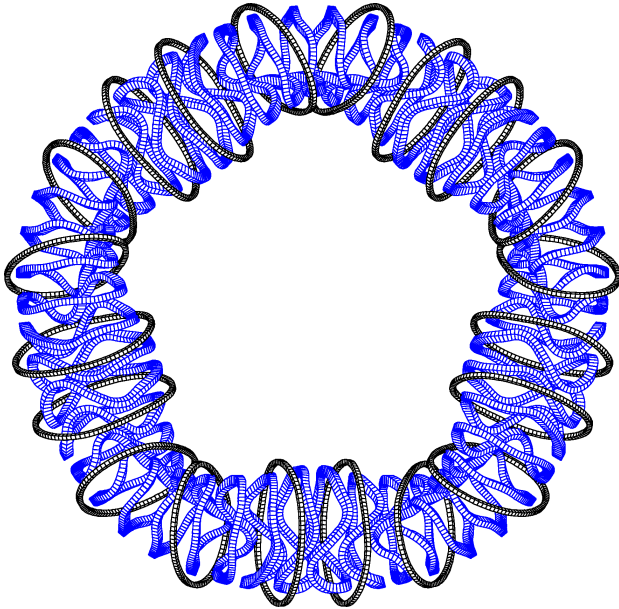
(a) *All 50 modular (blue) and 20 planar coils (black) [31]*
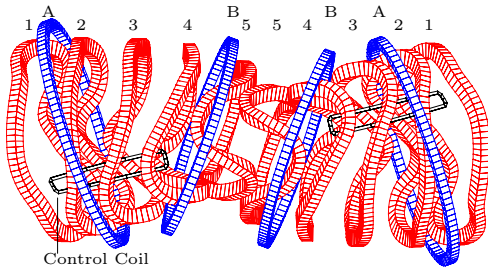
(b) *Coils contained in one module with modular coils 1 − 5 (red) and planar coils A, B (blue). Adapted after [32]*

Figure 6: *Overview of the W7-X main coil system*

$\bar{\iota}$ but these plasma effects can be effectively mimicked by adjusting coil currents [31]. In particular, the $\bar{\iota}$ changes due to plasma currents are roughly equivalent to changes caused by the currents I_A and I_B in the planar coil systems. While it is complicated and computationally intensive to calculate the plasma currents that change $\bar{\iota}$, it is straight-forward to calculate the essentially equivalent changes in $\bar{\iota}$ caused by I_A and I_B. For this reason, the NNs are trained to reconstruct the sum of the modular currents I_A and I_B of an $\bar{\iota}$-scan rather than reconstructing the toroidal plasma current.

Table 1: *Planar currents I_A and I_B of OP1.1 $\bar{\iota}$-scan experiment and simulation. The number of distinct configurations in the scan is labeled "# configs".*

	I_A	I_B	# configs
experiment	0.13	$[0.00, 0.13]$	6
simulation	0.13	$[-0.05, 0.18]$	1001

On 2016/03/09 several experiments were conducted, where a modest $\bar{\iota}$-scan was made (see e.g. [5]). I_B was varied from its standard OP1.1 normalized value of 0.13 (corresponding to 5 kA per turn), down to 0 while I_A was kept constant at 0.13. Strike lines from this experiment were also simulated(cf. 2.4.2) with a much closer spacing than that obtained with actual OP1.1 plasmas. The simulated data also extends this range by 0.05 in both directions. Table 1 lists the normalized currents of this experiment as well as those of the simulations.

2.4 Data Set Creation

In the following we discuss all steps necessary for the generation of NN training data. First the experimental IR data processing is discussed. Subsequently the process of strike line simulation is described. For several reasons, a post processing applied to both experimental and synthetic data is necessary before the data
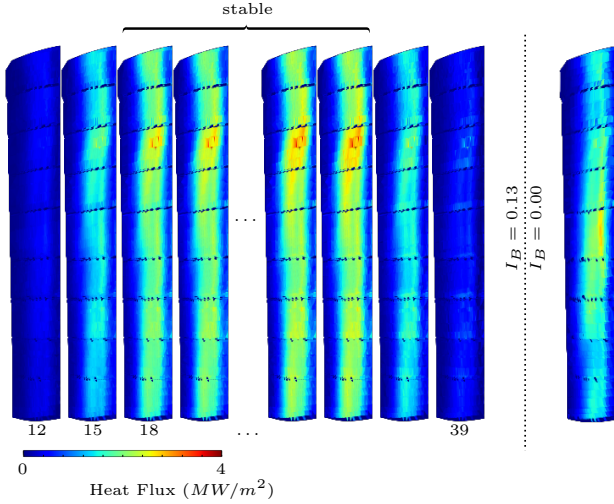
Figure 7: *Selection of eight frames from the DIAS diagnostic, recorded during discharge "20160309.007" at $I_B = 0.13$ in heat flux representation. The chosen frames (respective frame numbers written below) display the plasma build up and break down. For this experiment, a stable plasma-wall interaction occures from frame 18 till 34. The frames depicted only show that half of the limiter which was observed by the camera. For a comparison of strike lines at different I_B, one frame from discharge "20160309.035" ($I_B = 0.00$) is shown on the right.*

can be used as a NN input. This is elaborated in Section 2.4.3.

2.4.1 IR Data Processing

The OP1.1 $\bar{\iota}$-scan covers I_B specified in Table 2. As mentioned above, two IR cameras where installed in OP1.1 (cf. Figure 1b). One long-wavelength (8 - 14 μm) μ-Bolometer camera from the company DIAS, able to operate in a 3 T magnetic field and a mid-wavelength (3 - 5 μm) CCD chip camera from the company FLIR. Both observe only parts of the limiter while other parts are shadowed (obstructed views). The FLIR camera observes only the center of the limiter. The DIAS camera faces a full side of module 5 limiter (see Figure 8a).
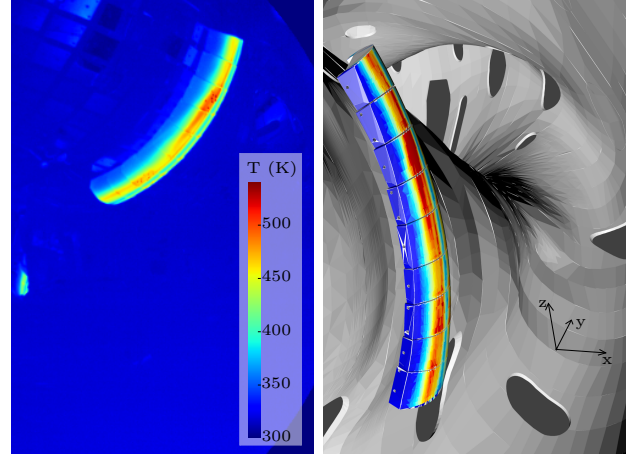
(a) *DIAS IR camera temperature data*

(b) *Limiter heat flux density corresponding to Figure 8a in three dimensions*

Figure 8: *Pseudo-color display of raw and processed data of discharge "20160309.007"*

Table 2: *Summary of available DIAS data for OP1.1 $\bar{\iota}$-scan from 2016/03/09. All modular coil currents were equal, that is $I_1, \cdots, I_5 = 1$. $I_A = 0.1300$ for all experiments of that day. I_B is given in the first column. The following column gives the number of discharges where reliable IR data were available. The column labeled "# frames" denotes the total number of frames with stable plasma-wall interaction, i.e. durable strike line.*

I_B	# discharges	# frames
0.1300	3	52
0.1083	2	35
0.0867	2	42
0.0433	2	40
0.0217	2	29
0.0000	5	121

Since the limiter strikeline is expected to be symmetric about the center of the limiter, observing one side of the limiter is sufficient to infer the full strike line. Thus we focus on the DIAS camera as an input.

Each IR video is processed in several steps to obtain the heat flux q (in W/m²) [33].

Mapping 2D to 3D In order to account for geometry effects, the sequence of such IR pictures is mapped onto the 3D CAD model of the limiter [34]. Result of this procedure is a 3D temperature map, assuming the surface to behave like a perfect black body with an emissivity of 1.

Emissivity correction In reality, the emissivity of graphite is smaller than 1. Furthermore, over the three months of OP1.1 the emissivity of the limiter tiles became nonuniform. This effect was explained in terms of surface layer depositions created during plasma operation [35], was quantified, and the data were corrected accordingly, yielding absolutely calibrated surface temperatures of the limiter as a function of time.

Heat flux This surface temperature is the result of the heat capacity and heat conductivity of the graphite combined with the time-history of the incident heat flux on the carefully shaped limiter surface. The THEODOR (THermal Energy Onto DivertOR) algorithm [36] utilizes the temperature-dependent material properties and the measured time-dependent temperatures to deduce the heat fluxes. This typically reveals a pair of strikelines on either side of the limiter, one of which is the subject of this analysis.

Interpolation As a last step, we interpolate the resulting discrete heat flux map to retrieve a continuous heat flux distribution on the limiter surface as shown in figures 7 and 8b.

Dark frames are removed. Furthermore, the plasma build up and break down is discarded
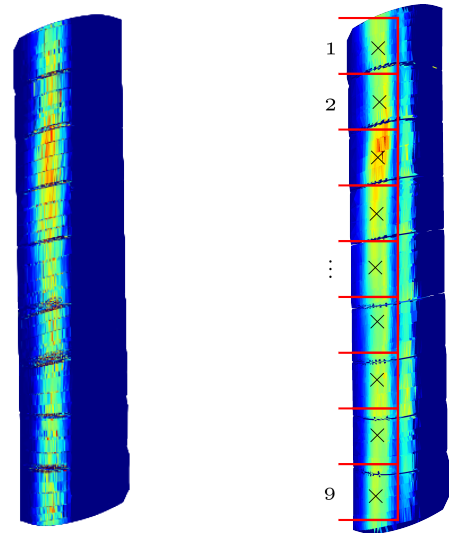
(a) *Heat load, represented by strike point density from a field line diffusion process*
(b) *DIAS camera data with nine regions defined for the NN input (enclosed by red lines) and $\mu(\vec{r})$ (black crosses)*

Figure 9: *Front views of heat load representations on limiter in module 5 at discharge "20160309.007".*

(see Figure 7). The remaining frames i. e. time spans of stable plasma-limiter contact, serve as the basis for further processing.

2.4.2 Strike Line Simulation

The size of the training data set strongly determines the performance of the NN after it has been trained. Since the amount of data for limiter operation is low, especially for the OP1.1 subset of the $\bar{\iota}$-scan (cf. Table 1), the data set is complemented by simulated strike lines. For the proof of principle, we make use of several approximations, described below. The input creation can be broken down into sequential parts.

$\vec{B}$ **creation** A fast algorithm based on the Biot–Savart law generates $\vec{B}$ from the W7-X coil currents. β-effects like Pfirsch-Schlüter currents can be neglected since

the discharge β are small yet, where $\beta = \frac{p}{B^2/2\mu_0}$ is the ratio of thermal to magnetic pressure. The coil geometry used was created by modifying the ideal coil set, taking into account preload and electromagnetic forces as well as dead weight cool down at modular coil currents of $6\,\text{kA}$ and planar coil currents of $2.3\,\text{kA}$ each [37].

Field line diffusion The approach to simulate particles and heat transport from the plasma core to the edge is as follows: Pseudo-randomly distributed particles are generated on the LCMS, assuming that the energy flux across the LCMS is uniform on the surface. Then particles follow their field lines, taking small random steps perpendicular to the field to simulate cross-field diffusion. If a particle trace intersects a material component the trajectory is stopped and the particle is registered as having hit the surface of the object through which the particle entered the object. The algorithm is described in more detail in [38], and it neglects the effects of magnetic drifts. The relevant parameters for the diffusion process are perpendicular diffusion coefficient $D_\perp$, collisional mean free path λ and velocity v. Values assumed for these constants are $D_\perp = 1\,\text{m}^2/\text{s}$, $\lambda = 0.1\,\text{m}$ and four different values for v between 1.4×10^5 and 2.8×10^5 m/s. They are empirically justified in [31, Chapter 3.3]. A number of 8000 diffusion traces proved to be fast as well as robust in terms of strike line characteristics.

DIAS emulation The strike zone is typically two strike lines, one on either side of the limiter. As only one side is fully covered by the DIAS view, the field diffusion points on the far side are mirrored (with stellarator symmetry: $x \to -x$, $z \to -z$) to that side. The simulation procedure described above provides the strike line heat load, represented by the strike point density (e. g. Figure 9a).

2.4.3 Strike Line Partitioning

To make the NN robust towards noise, averaging quantities are extracted from the strike line and serve as input.

The raw simulation and experiment data are significantly different because simplifying assumptions were made in the simulation (cf. Section 2.4.2). NNs trained on synthetic data but applied to reality may perform poorly. This problem is known in the machine learning community [39, Chapter 2.3.3].

In the following, processing steps are described to transform the simulated and experimental data sets in such a way that the NN can hardly distinguish them. The $80\,\%$ quantile is applied to the IR data as the threshold limit q_thr for the local heat load. For each triangle i on the CAD triangulated limiter, this threshold is implemented by setting $q_i = 0$ for $q_i < q_\text{thr}$. Each data set is split into nine regions, roughly following the natural geometry of the nine limiter tiles as shown in Figure 9b. For each of those nine regions, we compute the center of mass of the heat flux

$$\vec{\mu} = \frac{1}{\sum_{i=1}^{n} A_i q_i} \sum_{i=1}^{n} A_i q_i \vec{\kappa}_i, \tag{8}$$

with n triangles per section, where each triangle i has the properties centroid $\vec{\kappa}_i$, area A_i and heat flux q_i.

The NN inputs are

$$\Delta\vec{\mu} = \vec{\mu} - \vec{\mu}_\text{ref}, \tag{9}$$

with $\vec{\mu}_\text{ref} = \vec{\mu}(I_\text{B} = 0)$, separately for experiment and simulation. This processing is introduced in order to be independent of the origin of the coordinate system in each region and diminish the offset between the two data sets.

As an example, Figure 10 depicts all three spatial components of $\vec{\mu} = (\mu_x, \mu_y, \mu_z)^T$ for the section corresponding to tile 4. $\Delta\mu_x$ and $\Delta\mu_y$ show a similar behavior, except for a constant
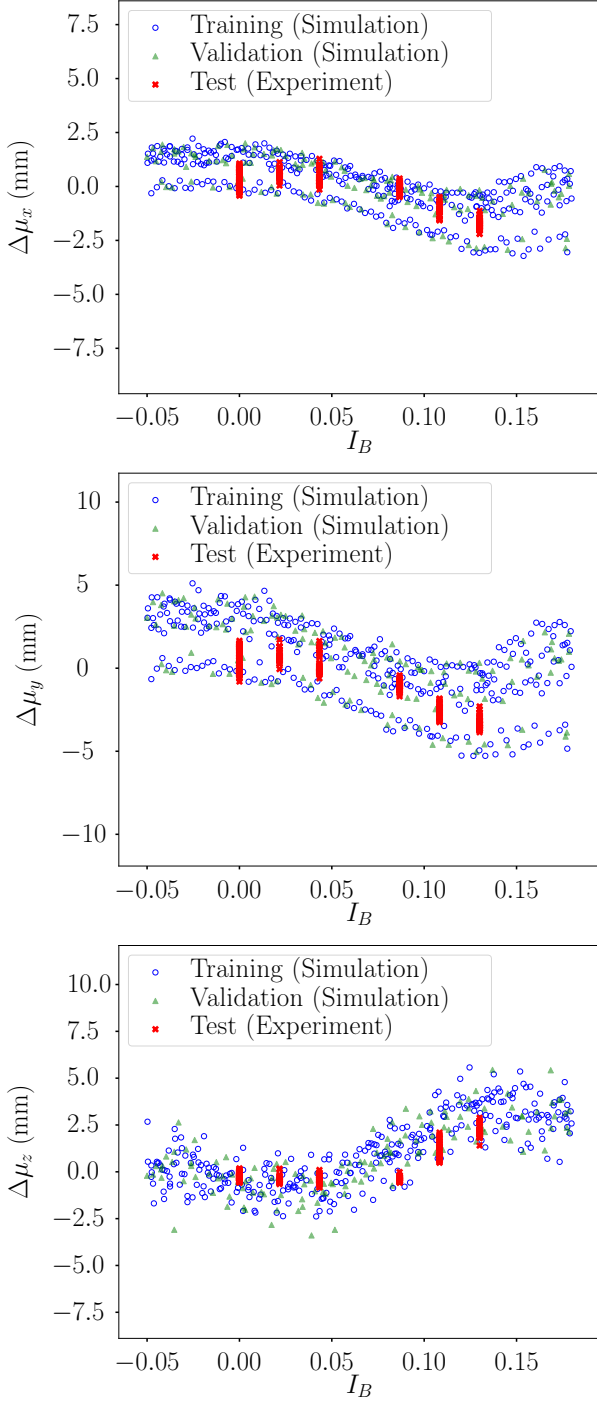
Figure 10: *The images show three different NN inputs depending on the planar coil current. The data presented in each graph are training set (blue), validation set (green) which are both based on simulations, and the experimental test set (red). The training and validation set are based on four different field line diffusion velocities to illustrate different collisionalities (cf. Section 2.4.2) which leads to distinguishable curves.*

scaling factor. Since the NN will rescale the input to a standard deviation of 1 (cf. 2.1), this factor vanishes. Thus only $\Delta\mu_x$ and $\Delta\mu_z$ are given to the NN. As expected, we observe systematic differences between simulation and experiment. For example, $\Delta\mu_z$ is slightly above the mean simulation result for $I_B < 0.05$ while it is below the simulation trend for the other half.

The variability of $\Delta\vec{\mu}$ stems from the random processes and different velocities used for field line diffusion simulation described in Section 2.4.2.

3 Results

In the following, we present the results of the I_B prediction. They were created with the same input parametrization (cf. Section 2.4.3) and NN architecture (see Section 2.1).

3.1 IR Data

A NN is trained and tested on all available IR data from the OP1.1 $\bar{\iota}$-scan. This means in particular, only six different I_B values are available for training, validation and testing. Figure 11 shows I_B, reconstructed from the strike line, in dependence of the actual target value of I_B. Here, as well as in all following figures, the NN validation is displayed by means of red circles. The independent test sets are depicted in terms of blue triangles. In case of an optimal reconstruction, target and NN output turn out equal, indicated by the dashed line. It can be seen that the NN is able to reconstruct I_B sufficiently well, since the points for the test set scatter closely and symmetrically around the target I_B. This is quantified by a *rmse* of only 0.010 for the validation as well as the test set. Because only six different magnetic configurations are available here, the NN is not expected to perform well for the interpolation between the
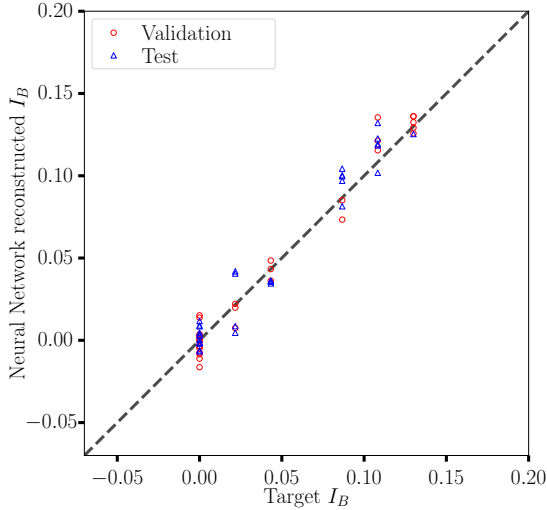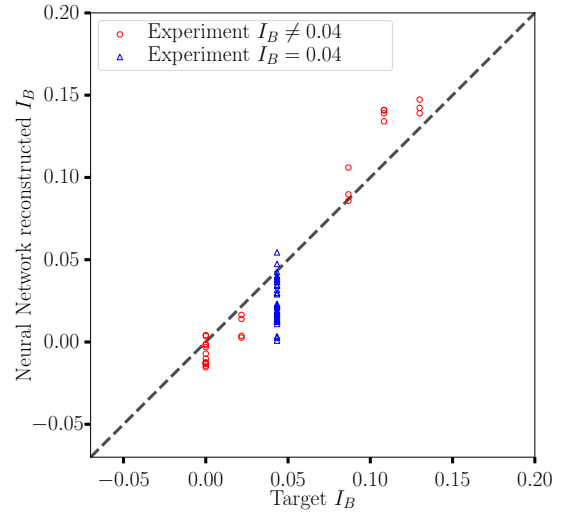
Figure 11: *NN performance, on IR data only. Red circles represent the validation set while blue triangles identify members of the test set.*

given currents. This can be seen in Figure 12a, where *rmse* for validation is 0.016 and 0.023 for the test set which is 40 % larger. As one might expect, the *rmse* for extrapolation differs by more almost one order of magnitude, namely 0.007 for validation and 0.047 for the test set. Figure 12b shows this behavior.

3.2 Combination of IR and Synthetic Data

To obtain a sufficient amount of training data, we simulate the limiter $\bar{\imath}$-scan described in Section 2.3. As with the previous result on experimental data, I_B is well reconstructed by a NN, trained with simulated data leading to an *rmse* of 0.014 in both validation and test set. Additionally, the NN trained with synthetic data can now be tested with IR data, i.e. in the process of training, the NN was never exposed to any subset of this test set, neither implicitly (validation set) nor explicitly (training set).

The test is performed with all DIAS frames

(a) *Interpolation performance, demonstrated by training and validating with five out of the six I_B, and testing on the remaining $I_\mathrm{B} = 0.04$*
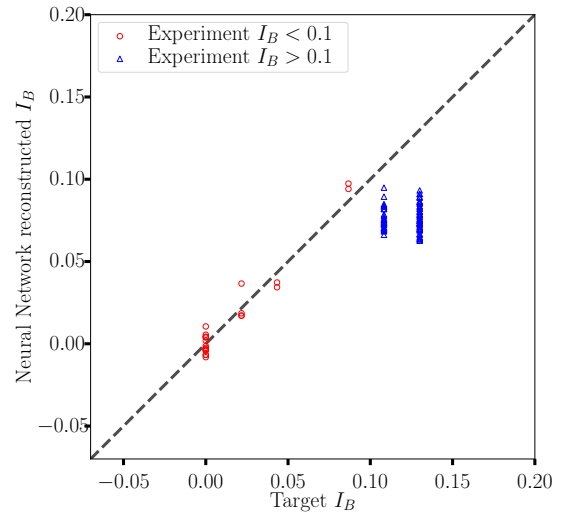
(b) *Extrapolation performance, demonstrated by training and validating with the lowest four out of the six I_B, and testing on the remaining two I_B values*

Figure 12: *NN performance on IR data corresponding to Figure 11. Red circles represent the validation set while blue triangles identify members of the test set.*

given in Table 1. The green squares in Figure 13a show the performance for this data set. The experimental data follow the trend of the dashed line with an $rmse$ of 0.029. We observe a small but clear and systematic underestimation of I_B of -0.026 ± 0.001 on average; this causes the larger $rmse$ as compared to the validation set. The reason for this offset is not yet clear to us but is under investigation. Though the test set does not perform as well as the validation set, the performance can already be considered a success, considering the relatively small discrepancies and the complexity of the problem (cf. Section 2.4.3).

We examine now whether training with a subset of experimental data improves the NN performance for such experimental data with no corresponding target I_B in neither training nor validation set. The only change as compared to Figure 13a is introduced by adding all IR data with target I_B below 0.1 to the training and validation set. This way, the NN should learn to neglect systematic differences between simulation and experiment. The discrepancy is significantly reduced as compared to the only simulation trained NN, quantified by an $rmse$ of 0.023. Still, the reconstruction underestimates I_B.

Note that the validation $rmse$ of 0.013 for this NN is similar to that of the NN presented in Figure 13a, although it is trained with a mixture of experimental and simulated data. In Section 3.1, we demonstrated the poor interpolation as well as extrapolation ability of the NN with few target I_B. The NN presented here clearly outperforms the extrapolation result discussed in Section 3.1.

4   Conclusion

It was shown here that neural networks are capable of reconstructing the magnetic configuration in terms of its $\bar{\iota}$ value, with experimental observations of limiter heat loads performed
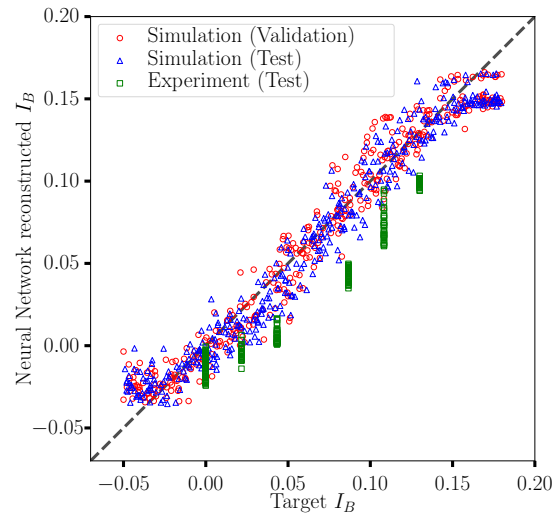
(a) *NN trained on simulation and tested with simulated and experimental data*
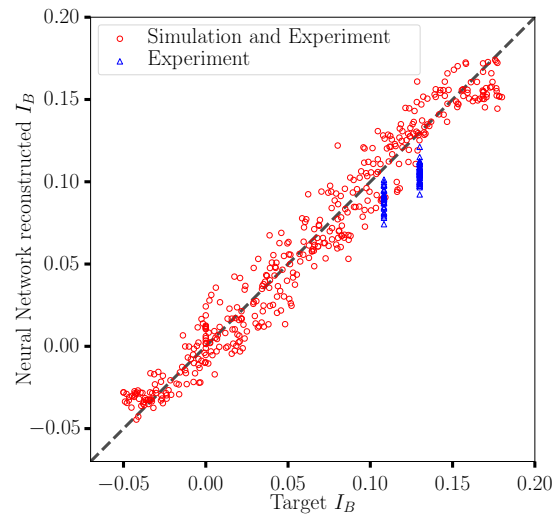
(b) *Training and validation set are supported by the full experimental data set with lower 2/3 of I_B to improve the reconstruction performance of the NN extrapolating towards upper 1/3 of I_B.*

Figure 13: *Performance of NN based on simulation data. Red circles represent the validation set while blue triangles and green squares identify members of the test set.*

during an $\bar{\iota}$-scan during the first experimental phase of Wendelstein 7-X. The NNs operated on real IR as well as simulated data. The NNs trained on simulated data can reconstruct configurations from IR data with sufficient accuracy. An even better performance is reached when the NN training set is based on a combination of simulated and parts of the IR data. It is expected that this approach will lead to a capability of extracting key physics parameters (of which $\bar{\iota}$ is perhaps the most important) in real-time in future divertor operation, based on IR camera data and possibly other diagnostic signals as well. Such a system would play a major role in a real-time divertor operation control system on Wendelstein 7-X.

Further improvements in the ensemble of NN architecture and the data parametrization are subjects of ongoing work. In the upcoming OP1.2 with installed divertors we plan experiments with iota scans and non-negligible I_{tor}.

5 Acknowledgments

Bibliography

[1] Jr. Lyman Spitzer. "The Stellarator Concept". In: *Physics of Fluids* 1.1958 (1958), pp. 253–264. ISSN: 00319171.

[2] G. Grieger and I. Milch. "Das Fusionsexperiment WENDELSTEIN 7-X". In: *Physik Journal* 49.11 (1993), pp. 1001–1005. ISSN: 00319279.

[3] Craig Beidler et al. "Physics and Engineering Design for Wendelstein VII-X". In: *Fusion Science and Technology* 17.1 (1990), pp. 148–168.

[4] J. Nührenberg and R. Zille. "Stable stellarators with medium β and aspect ratio". In: *Physics Letters A* 114.3 (1986), pp. 129–132. ISSN: 03759601.

[5] Thomas Sunn Pedersen et al. "Key results from the first plasma operation phase and outlook for future performance in Wendelstein 7-X". In: *Physics of Plasmas* 24.5 (2017), p. 055503. ISSN: 1070-664X.

[6] Hermann Renner et al. "Physical Aspects And Design of the Wendelstein 7-X Divertor". In: *Fusion Science and Technology* 46.2 (2004), pp. 318–326.

[7] J. Boscary et al. "Design improvement of the target elements of Wendelstein 7-X divertor". In: *Fusion Engineering and Design* 87.7-8 (2012), pp. 1453–1456. ISSN: 09203796.

[8] R Brakel et al. *Specification of design loads for in-vessel components of w7-x*. Tech. rep. PLM: 1-AC-S0005.1. Max-Planck-Institut für Plasmaphysik, 2017.

[9] Henri Greuner et al. "Cyclic heat load testing of improved CFC/Cu bonding for the W 7-X divertor targets". In: *Journal of Nuclear Materials* 386-388 (2009), pp. 772–775. ISSN: 00223115.

[10] Alan Peacock et al. "Status of High Heat Flux Components at W7-X". In: *IEEE Transactions on Plasma Science* 42.3 (2014), pp. 524–532. ISSN: 0093-3813.

[11] M. W. Jakubowski et al. "Development of infrared and visible endoscope as the safety diagnostic for steady- state operation of Wendelstein 7-X". In: *QIRT* 100 (2014).

[12] Christopher M Bishop et al. "Real-time control of a Tokamak plasma using neural networks". In: *Neural Computation*. Vol. 7. 1. 1995, pp. 1007–1013.

[13] Barbara Cannas et al. "Dynamic Neural Networks for Prediction of Disruptions in Tokamaks". In: *10th International Conference on Engineering Applications of Neural Networks (EANN 2007)* 284 (2007).

[14] Jakob Svensson. "Artificial Neural Network Modelling in Nuclear Fusion Research and Engineering at the HET Tokamak". Doctoral thesis. Royal Insitute of Technology Stockholm, 2000.

[15] Tom Michael Mitchell. *The discipline of machine learning*. Vol. 9. Carnegie Mellon University, School of Computer Science, Machine Learning Department, 2006.

[16] P. J. Werbos. "Beyond regression: New tools for prediction and analysis in the behaviorial sciences". PhD thesis. Harvard University, 1974.

[17] Christian Szegedy et al. "Going deeper with convolutions". In: *Proceedings of the IEEE Conference on Computer Vision and Pattern Recognition*. 2015, pp. 1–9.

[18] Kaiming He et al. "Deep residual learning for image recognition". In: *Proceedings of the IEEE Conference on Computer Vision and Pattern Recognition*. 2016, pp. 770–778.

[19] John Duchi, Elad Hazan, and Yoram Singer. "Adaptive subgradient methods for online learning and stochastic optimization". In: *Journal of Machine Learning Research* 12.Jul (2011), pp. 2121–2159.

[20] Diederik P. Kingma and Jimmy Lei Ba. "Adam: a Method for Stochastic Optimization". In: *International Conference on Learning Representations 2015* (2015), pp. 1–15. ISSN: 09252312. arXiv: 1412.6980.

[21] Sharan Chetlur et al. "cudnn: Efficient primitives for deep learning". In: *arXiv preprint arXiv:1410.0759* (2014).

[22] Martín Abadi et al. "Tensorflow: Large-scale machine learning on heterogeneous distributed systems". In: *arXiv preprint arXiv:1603.04467* (2016).

[23] James Bergstra et al. "Theano: A CPU and GPU math compiler in Python". In: *Proc. 9th Python in Science Conf.* 2010, pp. 1–7.

[24] Yann LeCun, Yoshua Bengio, et al. "Convolutional networks for images, speech, and time series". In: *The handbook of brain theory and neural networks* 3361.10 (1995), p. 1995.

[25] Henrique Steinherz Hippert, Carlos Eduardo Pedreira, and Reinaldo Castro Souza. "Neural networks for short-term load forecasting: A review and evaluation". In: *IEEE Transactions on power systems* 16.1 (2001), pp. 44–55.

[26] Alex Krizhevsky, Ilya Sutskever, and Geoffrey E Hinton. "Imagenet classification with deep convolutional neural networks". In: *Advances in neural information processing systems*. 2012, pp. 1097–1105.

[27] Olga Russakovsky et al. "Imagenet large scale visual recognition challenge". In: *International Journal of Computer Vision* 115.3 (2015), pp. 211–252.

[28] Xavier Glorot and Yoshua Bengio. "Understanding the difficulty of training deep feedforward neural networks." In: *Aistats*. Vol. 9. 2010, pp. 249–256.

[29] Ian H Witten et al. *Data Mining: Practical machine learning tools and techniques*. Morgan Kaufmann, 2016.

[30] P. I. Strand and W. A. Houlberg. "Magnetic flux evolution in highly shaped plasmas". In: *Physics of Plasmas* 8.6 (2001), pp. 2782–2792. ISSN: 1070-664X.

[31] H. Hölbe. "Control of the magnetic topology and plasma exhaust in the edge region of Wendelstein 7-X : a numerical study". PhD thesis. Universität Greifswald, 2016.

[32] T. Andreeva. *Vacuum magnetic configurations of Wendelstein 7-X*. Tech. rep. Greifswald: Max-Planck-Institut für Plasmaphysik, 2002.

[33] Holger Niemann et al. "First Power Decay Length Studies in the Limiter Phase of Wendelstein 7-X". Unpublished Manuscript. 2017.

[34] B Cannas et al. "Towards a new VIS/IR image processing system at W7-X: from spatial calibration to characterization of thermal events". Unpublished Manuscript. 2017.

[35] G. A. Wurden et al. "Limiter observations during W7-X first plasmas". In: *Nuclear Fusion* 57.5 (2017), p. 056036. ISSN: 0029-5515.

[36] A. and The ASDEX Upgrade Team Herrmann. "Limitations for divertor heat flux calculations of fast events in tokamaks". In: *Proc. 28th EPS Conf. on Controlled Fusion and Plasma Phys.* Vol. 25A. 2001, p. 2109.

[37] K Egorov. *ANSYS GM 504: FE Model Description*. Tech. rep. Greifswald: Max-Planck-Institut für Plasmaphysik, 2011.

[38] S.A. Bozhenkov et al. "Service oriented architecture for scientific analysis at W7-X. An example of a field line tracer". In: *Fusion Engineering and Design* 88.11 (2013), pp. 2997–3006. ISSN: 09203796.

[39] Jens Kober and Jan Peters. "Learning Motor Skills: From Algorithms to Robot Experiments". In: *Springer Tracts in Advanced Robotics* 97 (2014). ISSN: 1610742X.